

Upward Flux of Sublimation from the Surface of Ganymede

C.J. Alexander¹, S.J. Bolton¹, R. Carlson¹, W. Ip², J.R. Spencer³

¹California Institute of Technology /Jet Propulsion Laboratory, 4800 Oak Grove Dr.,
Pasadena, CA, 91109

²Max Planck Institute fur Aeronomie, Max-Planck Str. 2, D-37191 Katlenburg-Lindau,
Germany

³Lowell Observatory, 1400 Mars Hill Rd, Flagstaff, AZ, 86001

Number of pages: **50**

Number of tables: **2**

Number of figures: **11**

Submitted to Icarus 3.31.99

Key words: Ganymede; Geological processes; Surfaces, satellites; Satellites, atmospheres;

Regoliths

Proposed Running Head:

Sublimation from the Surface of Ganymede

Editorial Correspondence and proofs should be directed to:

Claudia J. Alexander

Jet Propulsion Laboratory

4800 Oak Grove Dr.

Pasadena, CA 91109

email: calexand@pop.jpl.nasa.gov

Tel; (818)393-7773

FAX: (818)393-4530

Abstract

Measurements taken by the Galileo plasma instrument when the spacecraft passed Ganymede at an altitude of only 261 km indicated the presence of a supersonic outflow of gas composed solely of H^+ (Frank, et al., 1997). The source of this gas is likely to be water vapor and other molecules sputtered from or sublimated from the surface. The model presented here is a preliminary look at processes near the surface which may lead to the formation of the atmosphere. A comet nucleus thermal model has been altered to calculate the temperature distribution on the satellite surface and to address the question of sublimation from the surface. The thermal model is an integration of a 1-D heat conduction equation for a selected subset of Ganymede longitudes over a diurnal cycle. Voyager albedo measurements were used to constrain the surface thermal model. Surface brightness temperatures from the Galileo Photopolarimeter Radiometer (PPR) experiment were used both to estimate the extent of varying terrain types in the area, and to constrain the calculated surface temperatures. Preliminary results show a maximum (noon) subsolar surface temperature of 153 K, extensive regions of vigorous sublimation, and a total global water production from (upward) sublimation of $\sim 10^{26}$ molecules/s.

1. Introduction

Galileo encounters with Jupiter's icy moon Ganymede produced the surprising discovery of what can loosely be described as an atmosphere. At an altitude of only 261 km, the Plasma Science (PLS) instrument registered the presence of a gas composed of singly ionized hydrogen flowing away from Ganymede at supersonic speeds. Other recent detections of volatiles near and in the surface of Ganymede suggest intriguing possibilities for the source of the tenuous atmosphere/exosphere which Ganymede seems to possess. Measurement of the spectral signatures of O_2 as well as O_3 from the satellite surface by

ground based observers [Spencer et al., 1995, Calvin et al., 1996, Noll et al., 1996], suggest that volatile oxygen, of uncertain origin, may be trapped within the near surface icy layers of Ganymede. Hall et al. [1998] report the finding of an atomic oxygen emission from the atmosphere of Ganymede which is spatially inhomogeneous. The mechanism proposed for the creation of this emission, namely electron dissociation of O_2 to produce excited atomic oxygen, suggests the presence of significant background levels of O_2 . Galileo Ultraviolet Spectrometer (UVS) observations demonstrated the presence of sufficient atomic hydrogen near Ganymede [Barth, et al., 1997] for exospheric models extending from the surface to suggest a surface density of $1.5 \times 10^4 \text{ cm}^{-3}$, scale height of 2634 km, and a gas temperature of 450 K. The UVS data is also consistent with an exosphere modeled as freely escaping hydrogen.

Speculation about the origin of the atmosphere includes; sublimation of water vapor from the surface of Ganymede, sputtering of water and other ions from the surface, and perhaps diffusion of volatiles from mini-atmospheres found in “bubbles” in the icy matrix which comprises the surface. In the scenario of a sublimated or diffusion created atmosphere, the observed flux of H^+ seen by the Galileo PLS instrument may be explained by separation of sublimated water vapor into its constituent family of molecules, H^+ , O^+ , H_3O^+ , O_2^+ , H_2O^+ , etc. (the “water group”), and acceleration of H^+ to escape velocities. Alternatively, H may be sputtered from the surface with sufficient energy to escape. Laboratory measurements suggest that sputtering agents may be able to release H_2O , H_2 , H, and O from the surface [Shi et al., 1995, Bar-Nun et al., 1985]. Water vapor associated with the surface via sublimation or sputtering would acquire energies consistent with the surface; namely 150 K. The significant escape flux measured by PLS suggests, since water must be the ultimate source of the atmosphere, a mechanism in which a large amount of oxygen is left behind.

The objective of this study is to contribute to understanding the sources and the processes leading to the substantial hydrogen escape with an examination of the role of sublimation. A preliminary model of near surface sublimation is presented for a restricted area of the Ganymede surface only; the region spanning -80° to $+10^{\circ}$ in latitude and 260° to 180° in longitude. The region is outlined in Fig. 1. For the purposes of this study, the region will be designated G1_S_hemisphere. Data from the region were taken on the first Galileo encounter with Ganymede (designated G1) concurrently by both the Galileo Photopolarimeter Radiometer (PPR) experiment, and the Near Infrared Mapping Spectrometer (NIMS). The data encompass local times from dawn to noon. A quantitative estimate of the flux of molecules from sublimation as well as the temperature of the surface is provided by the model based on current estimates of surface microtexture, porosity, and composition. The thermal model is constrained by albedo measurements from Voyager, PPR surface brightness temperatures, and ground based eclipse radiometry data on the thermal inertia.

2. The Surface Properties and Regolith of Ganymede

Sublimation of a surface is related to the temperature of the surface through the interface with the surface crust; both the thickness of the surface layer and its composition and thermal properties affect sublimation. Latent heat is released when ice held within the crust transforms to a vapor, cooling the crust, an effect which feeds-back to the surface temperature. A calculation of equilibrium surface temperature and sublimation is dependent upon factors which are unknown at this time including; the microtexture of the regolith, its porosity, grain size distribution, and shape. A discussion of these and other free parameters of the model follows in a later section. In this section we discuss the surface water ice abundance and distribution. The amount of sublimation to be expected from the

icy surface of Ganymede is a function of the transformation of ice to vapor and as such is dependent upon the amount of ice available for the phase change. However, the magnitude of the expected flux will be critically dependent upon the temperature of the surface, a factor which in turn may be critically dependent upon the amount of exposed ice at the surface in any given area. Spencer, [1987] showed that icy surfaces on airless bodies are susceptible to preferential removal of ice via sublimation from darker areas, and collection of ice in brighter, colder patches. The scale length of the segregation is on the order of kilometers to centimeters. In this model, the surface will be treated as a crudely segregated one, after Spencer, [1987]. The model separates regions into icy, moderately icy, and non-icy on a scale size of $10^\circ \times 10^\circ$. Such a size scale does not truly approximate a segregated surface, making the process of identifying icy regions unsatisfactory in this initial calculation, and will be revisited in future work. The surface of Ganymede can broadly be characterized, as per images returned by the Galileo Solid State Imager (SSI), as bright and dark terrain [Belton, et al., 1996]. Dark terrain is considered to be a primordial impact-generated surface covered with a dark contaminant [Prockter, et al., 1997], and the bright terrain seems to be characterized by imbricate faulting, that is blocks of ice with a vertical scalelength of ten's to hundreds of kilometers which, under forces of tectonic deformation lean together like fallen dominoes. The exposed surface of these blocks seems to be contaminated with a dark substance as well [Pappalardo, et al., 1997, Weitz, et al., 1997]. The outermost crust of the dark material may be very porous, on the order of 50% [Pappalardo, personal communication]. Both types of surface suggest the presence of a surface veneer which may not descend deeply into the regolith but which may affect the sublimation properties near the surface, particularly in bright terrain which contains a significant weight percent of ice such as that of Uruk Sulchus.

Band shapes and depths of spectra of water on the satellite surface obtained by ground based measurements are consistent with H₂O surface ice on Ganymede with grain sizes of a few hundred micrometers to 1mm (Cruikshank, et al., 1997, Buratti, 1991, Buratti, et al., 1988). These studies seem to suggest that while H₂O is the principal constituent of the surface of these satellites, a single particle size is probably not a suitable model for the surface ice. A representative sample of the global Ganymede surface returned by the Galileo NIMS is shown in Fig. 2. Figure 2a shows spectra returned from the very icy Osiris Crater and also from the very dark Marius Regio region. These spectra show strong absorptions in the characteristic water ice bands of 1.5 μm and 2.0 μm at both Osiris and Marius Regio. The depth of the bands indicates the strength of water absorption, an indicator of water abundance. Since NIMS can measure spectra of surface components to a depth of $\sim 10 \mu\text{m}$, absorption features at both of these terrain extremes suggest that there is a large amount of ice exposed to the surface nearly everywhere around the globe. Figure 2b shows comparative depths of the 2.0 μm band and a 4.25 μm feature around the satellite in three images, the left being a visible Voyager image of Ganymede, the middle being the 2.0 μm feature, and the rightmost being the 4.25 μm feature. The 4.25 μm feature is caused by an as-yet undetermined non-ice mineral, the 2.0 μm feature is another ice absorption feature. As suggested by the mottled appearance of the 2.0 μm and 4.25 μm features, band depths (described in detail by Carlson, et al., 1996) vary around the globe. While ice seems to be present everywhere, variability in the intensity and strength of absorption indicate that the amount of ice may vary locally, to the very least at the scalelength of NIMS resolution of 100's of kilometers. The 2.0 μm feature seems to be anti-correlated with the 4.25 μm feature and suggests, where the 4.25 μm feature is strong,

a surface either covered with a dark contaminant or depleted of ice. Areas which are dark at 2.0 μm seem to occur at low latitudes, and seem to correlate well with the dark features (ancient terrain) seen in data at visible wavelengths, shown in the leftmost hemisphere of Fig. 2. Together the observations suggest that the regolith is not made of a homogeneous mixture of ice but contains a significant non-ice component with grain sizes of a few hundred microns to millimeters and possibly very porous.

A more complete characterization of the regolith from NIMS data than those in the initial findings is required in order to better understand the local temperature field. Such a study will be performed in future work. Absolute abundances of icy and non-ice components are unknown at this time. The amount of water ice contributing to NIMS spectra can be modeled by radiative transfer considerations however there is quantitative difficulty differentiating between linear mixtures (i.e. checkerboard or areal mixing) versus that of intimate mixtures of ice and rock. Early NIMS analysis of ice abundance has been hampered by the lack of determination of the ice grain size. Band depth maps for non-ice absorption features have been produced for the surface of Ganymede (McCord et al., 1998), however there is ambiguity in identifying the absolute abundance of the end member units. Since knowledge of the ice abundance is crucial to this study, approximate guesses about the ice abundance and distribution were made. The hemisphere under study, G1_S_hemisphere was divided into terrain types of composition ranging from 100% ice to 20% ice, where the concentration of ice in each terrain type was somewhat arbitrarily assigned. Two methods were used to make a determination of the terrain type. PPR temperature data from the G1_S_hemisphere (described in detail by Orton, et al., 1996) were used as an initial means of separating the surface into icy regions and less icy regions. These data are shown in Fig. 3a and 3b. The data show temperatures ranging from 80 K to 150 K as the surface encompasses local times from dawn to noon. A preliminary analytical

estimate of the surface temperatures was provided by a model which solved the heat flux equation (Eq. 1) using Voyager albedos, after Sqyures, [1980]. The surface area of Ganymede was divided into polar and equatorial stripes, where the polar regions carried an albedo of 0.4 and the equatorial region carried an albedo of 0.2. The temperature field found by this method of calculation is shown in Fig. 3c. Subtraction of the initial diurnal temperatures from the PPR data, Fig. 3d, allowed a crude identification of regions which are colder than the surrounding surface. There were two such regions, the principal one being bright ejecta near the Osiris crater. It was assumed that these are regions which contain more ice than their surroundings, and were designated terrain type I for pure ice. Because the initial diurnal temperature calculation was based upon crude estimates of albedo, the figure shows that the measured temperature data departs from the predicted temperatures toward the poles.

An alternative means of characterizing the surface and validating the choices of terrain type from the PPR mosaic of G1_S_hemisphere came from the use of Voyager albedo data derived from spectral reflectances at visible wavelengths from the clear filter of the imaging camera (0.47 μm) at $1^\circ \times 1^\circ$ resolution. These data are shown in Fig. 4. Bright areas within an albedo contour of 0.35 and roughly aligned with the cold regions identified in the PPR data were labeled terrain type I for 100% ice. A region along the 0.25 contour, roughly south of -50° latitude was designated terrain type II. A region north of the 0.25 contour, between -50° and $+10^\circ$, with the exception of Uruk Sulchus, was designated terrain type III. An icy surface designated terrain type I corresponds to pure ice directly exposed to the surface. In practice, for now, this terrain encompasses only to very large-scale, high albedo features such as the Osiris Crater but might in later calculations also correspond to Palimpsests such as Memphis, Buto, or Achelous Facula, and isolated knobs in dark terrain. Icy surfaces designated terrain type II correspond to regions which can be

characterized as an ice/rock mixture, with an ice/rock ratio of perhaps 50%; bright terrain such as Uruk Sulchus formed of blocks of tilted and deformed lithosphere which are silicate poor but in which clean ice surfaces have been exposed. Icy surfaces designated terrain type III correspond to ice/rock mixtures with perhaps 20% ice; dark terrain (~50% of surface), considered to be a nearly primordial surface, in which the ice is covered by a thick veneer of dark contaminant. An example of this terrain would be Galileo Regio. The concentration of ice in these regions is a guess at this time.

3. The Surface Thermal Model

The thermal model is an integration of the energy balance equation inward from the surface

$$\frac{(1-A)}{d^2} \cos(i) \cos(\zeta) J = \sigma T^4 + \frac{\partial}{\partial z} \left(\kappa(T, \varphi) \frac{\partial T}{\partial z} \right) \quad 1$$

where A is the Bond albedo for visible wavelengths, J is the solar insolation, d is distance in AU, i is the solar incidence angle at the surface of Ganymede, ζ is the solar phase angle, σ the Stefan-Boltzmann constant, T the surface temperature, κ the thermal conductivity and z is the vertical direction. As heat is integrated inward, the regolith separates into volatile filled and volatile empty as if a “sublimation front” had passed through the near surface layer. At the sublimation front interface, the following energy balance equation holds

$$\frac{\partial}{\partial z} \left(\kappa(T, \varphi) \frac{\partial T}{\partial z} \right) = -L(T) \frac{\partial m}{\partial t} \quad 2$$

where m is the mass of the ice, and $L(T)$ is the latent heat of sublimation is a constant function of temperature (after Houppis, et al., 1987, and Newitt et al., 1956) of 5.0×10^{11} ergs/mole. Eq. 2 reflects the fact that the change of mass which occurs when latent heat is released during sublimation is equivalent to the heat flux being conducted inward.

Integration of (2) over the vertical distance, z , implies the formation of a mantle of thickness, Δ . Time dependence of the model is carried by the mass-change term, $\partial m/\partial t$, a term which is related to the size of the overlying mantle and is properly a function of the difference between the upward molecular flux and the return flux. Given a surface atmosphere empty of molecules, a molecule released from the surface via sublimation will make a transit across the surface [Sieveka and Johnson, 1982]. The distance traveled on the excursion may be as little as 100 km or as large as 2500 km, and may be a function of local time. Thus the upward and downward fluxes at a single grid point may not be equivalent. In this preliminary model, the mass change term will be taken as a pre-assigned constant, and Δ will be a free parameter (discussed later) of fixed but arbitrary size. In future work, when the downward molecular flux into the mantle is better understood, $\partial m/\partial t$ will be solved self-consistently as a function of the return flux. Time dependence of the temperature field, nominally written as $(1/\rho C_p)\partial T/\partial t$ on the left hand side of Eq. 1, is irrelevant to this initial model regardless of the fact that diurnal temperatures are being calculated. The time dependent temperature contributes to a lag in the peak surface temperatures relative to local noon and will not be considered here. The thermal conductivity is both a function of porosity and temperature, as discussed below.

The thermal conductivity of pure ice is an inverse temperature dependent function, after Klinger [1987]

$$\kappa_i(T) = \frac{\alpha'}{T} \quad 3$$

where α' is 5.67×10^7 ergs/cm²/s. The thermal conductivity of a mixture of ice and rock is taken to be a volume average of the two conductivities, after Kossowski et al. [1997]:

$$\kappa_c(T, \varphi) = \rho_c(\varphi) \left(\kappa_i(T) \frac{1 - c_m}{\rho_i} + \kappa_r \frac{c_m}{\rho_r} \right) \quad 4$$

where ρ_c is the conglomerate density, a function of porosity, φ , c_m is the concentration of rock within the regolith, κ_r is the thermal conductivity of rock, taken to be a constant 60 ergs/cm²/s/K [Houppis, et al., 1987, Fountain and West, 1967], ρ_i is the density of pure ice Ic, 0.92 g/cc, and ρ_r is the density of rocky component, taken to be 3.44 g/cc. The conglomerate is an admixture of ice and rock where the degree of mixing was indeterminate, that is no distinction was made between an intimate mixture of ice and rock, and a more areal mixture. In the next section we will examine the influence of the first and second terms inside the parenthesis of Eq. 4 (terms One and Two, respectively) for the roles they play in the overall volume averaged conductivity.

The thermal conductivity of the gaseous flux is

$$\kappa_g(T, \varphi) = \frac{r_p}{\tau^2} \varphi \left(\frac{32\mu_i}{2\pi RT} \right)^{\frac{1}{2}} L_i(T) \frac{dP}{dT} \quad 5$$

[Kossaski, et al., 1997, Smoluchowski, 1979] where μ_i is the molar mass of water vapor, R is the universal gas constant, $L(T)$ is the latent heat of sublimation, and P is the vapor pressure in the pores. The assumed thermal conductivity of (solid) porous ice with no contribution from vapor contained in the pores, κ_s , is taken to be, after Kossaski et al. [1997]:

$$\kappa_s = \kappa_c h(1 - \varphi)^{\frac{1}{3}} \quad 6$$

and accounts for increase of thermal conductivity with decrease in porosity, where the power of 2/3 is obtained from geometrical considerations regarding the packing of equal spherical grains. The Hertz factor, h , is given as the ratio squared of the contact area between the grains, r_n to the crosssection of a single grain, r_g , and varies with porosity as shown in Eq. 6 [Swinkels and Ashby, 1981]. The hertz factor can be considered a time dependent function when accounting for the re-condensation of material within the regolith. The effective conductivity of two phase materials, where κ_s is the conductivity of the solid, and κ_g is the conductivity of the vapor phase is as follows:

$$\bar{\kappa} = \frac{3\kappa_s\kappa_g\phi + (2\kappa_s + \kappa_g)(1-\phi)\kappa_s}{3\kappa_s\phi + (2\kappa_s + \kappa_g)(1-\phi)} \quad 7$$

[Smoluchowski, 1989, see also Kaviani, 1991]. With large pores and high temperatures, heat conduction by vapor contained within the pores by both viscous (free sublimation) and Knudsen flow becomes important. In this model, the temperatures are not high enough for physical effects from Knudsen flow within the regolith to be considered. Nevertheless, the thermal conductivity is modeled to account for these effects with time dependent pore sizes, porosity, and hertz factor.

4. Sublimation

The mass change which occurs as a result of sublimation leads to the release of latent heat. This mass change is related to the gas production as follows

$$dq = L(T) \frac{dm}{dt} = \left(\frac{L(T)f\dot{Z}}{N_A} \right) \quad 8$$

where, in both gas flow regimes discussed below, the gas production rate, \dot{Z} , is the mass flux; $\dot{Z} = nm\dot{u}$, and a Maxwell-Boltzmann distribution close to equilibrium effectively describes the velocity distribution of the gas. For gaseous flow in the Knudsen regime, the mass flux percolates through N_p (cylindrical) pores. Thus

$$\dot{Z} = nmN_p \frac{4}{3} \sqrt{\frac{2kT}{\pi m}} \quad 9$$

Here, u is the most probable speed,

$$u = \sqrt{\frac{2kT}{\pi m}} \quad 10$$

n comes from the Clausius/Clapeyron equation (after Houppis et al., 1985), and $4/3$ is a geometric factor which accounts for the permeability of the layer (see Present, 1958, and also Mason and Malinauskas, 1983]. N_p is the volume of the mantle at a given grid point, A , divided by the volume of cylindrically shaped pores of diameter πr_0^2 and length $\tau_m \Delta$;

$$N_p = \frac{A}{\pi r_0^2 \tau_m \Delta} \quad 12$$

where τ_m is the tortuosity of the pores, a factor which effectively lengthens the pore, and r_0 is the pore radius.

For free sublimation to space, there is no lag deposit therefore N_p is set equal to 1 as if the length of the pores is infinitely small, and u is taken from the mean translational energy of a molecule in a single species gas;

$$u = \sqrt{\frac{\gamma k T}{m}} \quad 13$$

where γ is the specific heat for water vapor. Thus, for free sublimation to space

$$\dot{Z} = nm \sqrt{\frac{\gamma k T}{m}} \quad 14$$

5. Sensitivity Studies with the Model

The list of free parameters associated with the model includes the albedo of the surface, the emissivity, the bulk density of the material, the thermal conductivity of the material, pore radius, tortuosity, and the mantle thickness. Selected values for these parameters are listed in Table 1. Factors related to the microtexture such as the pore radius, tortuosity, and emissivity cannot be modeled accurately without a detailed physical model of the regolith. In particular, emissivity, which is a function of pore radius and depth, was scaled according to the assumed porosity and tortuosity of the matrix at any given time, and the pore radius was scaled according to the porosity and hertz factor, constrained by the eclipse radiometry data. Since so many parameters are indeterminate, sensitivity studies were performed with the model using a range of values for each of the above listed parameters. A discussion of the values chosen for these parameters follows below.

As described earlier, we somewhat arbitrarily chose the concentration of ice in the terrain types to be 100%, 50%, and 20% respectively. With future work we expect these estimates to be refined or change completely. Nevertheless, as a first approximation these estimates should serve to provide an adequate range of possible terrain microtextures from which sublimation rates can be derived. Similarly the porosity of the terrain was somewhat arbitrarily chosen. Constraints on thermal inertia provided by eclipse radiometry data

limited the estimates of porosity to no more extensive than 50%. The amount of sublimation to be expected at any given time from the regolith will be dependent upon the thickness of the overlying mantle, or layer of material more or less depleted of volatiles for sublimation. The thicker the mantle the greater the insulation and the greater the blanket of material through which a gas must pass to escape the regolith. Thus, as sublimation proceeds, a mantle will thicken with a negative feedback effect. A thick mantle will have a tendency to choke off continued sublimation. Future version of this model will self-consistently calculate the varying thickness of the mantle with local time. In this preliminary model mantle thicknesses, Δ , are assumed to be fixed and have pre-assigned values ranging from 2 μm to 20 cm. The values of Δ imply something about the relative magnitudes of the downward flux, but for now there is no physical association of Δ with downward flux. The values 2 to 200 μm were chosen to be associated with what Noll et al., [1996] describes as the excited skin of the Ganymede surface where expected chemical interactions between the surface and the atmosphere take place. Other values of mantle thickness used by the model are listed in Table 1.

The surface temperature obtained from the calculation is critically dependent upon the chosen albedo. The bond albedo used was obtained from geometric albedos derived from the Voyager PDS clear filter (0.47 μm) with a lunar-Lambert photometric correction applied. The geometric albedos range from 0.17 to 0.36 and cover G1_S_hemisphere at $1^\circ \times 1^\circ$ resolution. These have been binned to $10^\circ \times 10^\circ$ resolution for use with the model's numerical grid. The Bond albedo was obtained from the geometric albedo through an approximation to the phase curve of the Ganymede surface, as given below and described by McEwen [1991].

enhanced. For G1_S_hemisphere, the maximum geometric albedo was 0.36. Application of the phase correction brings the albedo of the surface closer to values employed by Squyres [1980], as shown in Fig. 6.

In the absence of knowledge of the microtexture and porosity of the surface, two gas flux regimes were modeled; free molecular flow (Knudsen regime) and free sublimation to space (viscous regime). The former is appropriate for a regolith in which a liberated molecule makes more collisions with the walls of the surrounding micropores than with other liberated molecules. In this regime, the pore diameter acts as an effective mean free path. The latter regime is appropriate for a regolith in which the overlying crust is thin with respect to the scale length for collisions (the pore radius). The transitional regime wherein the pore size is of the same scale as the mean free path is a difficult one to model, thus for this calculation it will be assumed that, if the dimensions of the problem become such that the pore radius (r_0) is of the order of the pore length (Δ), then the flow description must revert to that for viscous flow.

Thermal conductivity as discussed in the previous section is a time dependent function of porosity and composition. The primary contribution to thermal conductivity comes from the conductivity of the solid matrix, as described by Eq. 6, where the thermal conductivity of the conglomerate is described by Eq. 4. Equation 4 contains three terms which will be designated; conglomerate density, One, the first term inside the parentheses, and Two, the second term inside the parenthesis. One describes the thermal conductivity of the icy portion of the conglomerate. Two describes the thermal conductivity of the rocky portion of the conglomerate. To test the sensitivity of the model, 9 thermal regimes were tested; ranging in composition from 100% ice, 50% ice, and 20% ice, and porosity from non-porous, 20% porous, and 50% porous. The effective thermal conductivities for these

$$\frac{I}{F} = f(\zeta) \left[2L(\zeta) \left(\frac{\cos i}{\cos i + \cos e} \right) + (1 - L(\zeta)) \cos i \right] \quad 15$$

where i is the incidence angle, e is the emission angle, $f(\zeta)$ is a phase-angle dependent function which expresses scattering properties peculiar to the surface of Ganymede, and L is an empirical limb-darkening parameter whose phase-angle dependent values are listed in Table 2. This correction of Eq. 15 accounts for the contribution to the variation in brightness from the directional scattering properties of the body as a function of solar phase angle. The functional dependence of $f(\zeta)$ may be $[1 \pm \cos(\zeta)]$ for preferential backward or forward scattering respectively, after Hapke, [1981] or may have a form introduced by Henyey and Greenstein [1941] in which

$$f(\zeta) = \frac{1 - g^2}{(1 + g^2 + 2g \cos \zeta)^{3/2}} \quad 16$$

where the asymmetry parameter $g = \langle \cos \zeta \rangle$. The effects of the function $f(\zeta)$ on the efficacy of the correction are most pronounced when the angle of incidence approaches 90° (Squyres and Veverka, 1982). Squyres and Veverka [1982] present a value of -0.3 for the asymmetry parameter for the Ganymede surface. In this calculation $f(\zeta)$ has a value of unity, expressing an assumption of isotropic scattering for the surface. This assumption may depart from reality significantly when the angle of incidence approaches 90° , a fact which may be reflected in the differences between the modeled temperatures and the data, described later. The emission angle was assumed to be 90 degrees. Figure 5 illustrates the effects of the Ganymede phase curve as described in equation 15 which corrects from geometric or normal albedo to Bond albedo. The phase curve lowers the albedo at high phase angles and raises the albedo at small phase angles. The phase curve also raises the normal albedo at high latitudes where the incidence angle is low. The effects of the phase correction are not linear. As the normal albedo increases, the effects of the phase curve are

conditions are shown in Fig. 7. (Variation in One & Two is also shown) It can be seen from Fig. 7 that 100% ice is the most conductive, 20% ice the least conductive. The increase in porosity lowers the effective conductivity of the matrix. The figure illustrates that the model thermal conductivity is not a linear relationship with ice content. The conglomerate density increases rapidly with increasing rock content (see Table 1), thus the effective conductivity of a conglomerate composed of 50% ice is larger than either of the other cases involving different ice composition. Figure 7 also shows corresponding thermal inertias calculated for the differing terrain types using these thermal conductivities. Thermal inertias for the model fall close to the range expected from global Ganymede eclipse radiometry data, of $1.02 - 1.56 \times 10^{-5} \text{ K cm s}^{1/2}/\text{ergs}$ [Hansen, 1973, Morrison and Cruikshank, 1973].

To test the sensitivity of the model, variations in parameter space were performed. The nominal area was assumed to be a hemisphere illuminated under a solar flux which ranged in phase from dawn to noon, in which the albedo varied as provided by the Voyager data, but which in all other respects was uniform. The integration proceeds via calculation of the temperatures, thicknesses, and sublimation rates for each grid point as the grid rotates through a Ganymede day, including differences with terrain type, and thermal conductivity. The model chooses the appropriate thermal regime based upon the designated terrain type. In the present model the porosity of the layer is invariant, and the size of the lag deposit is fixed with values given in Table 1. There is no heat conduction between grid points of the calculation. For this uniform area the 1) terrain type (composition), 2) mantle thickness, 3) gas flux regime, 4) emissivity, and 5) porosity were varied against each other in a systematic way. In all 540 runs of the model were performed, where each of the five parameters listed above carried a different expression. The range of values for each parameter is listed in Table 1.

A summary of the sensitivity study is shown in Fig. 8a, and b. In Fig. 8a the maximum temperature, gas flux, and total production for cases of the same terrain type (terrain type II), but different gas flux regimes, thermal (porosity) regimes, and differing mantle thicknesses are compared. The heavy black line indicates PPR maximum surface temperatures, and PLS measured escape flux respectively. Variations in emissivity drive the temperature up by a direct factor of the difference between the value of emissivity and unity, and these variations are not shown. In Fig. 8b, the maximum gas flux for cases of the same thermal (porosity) regimes (50% porosity), but different gas flux regimes, terrain type, and differing mantle thicknesses are compared. The comparison shows that there are some mantle thicknesses employed by the test where the upward flux is not produced with a magnitude comparable to the measured escape flux. The comparison also shows that terrain type III with 50% porosity and a mantle thickness of .02 centimeters provides more sublimation than that of terrain type I in a non-porous realm and a mantle thickness of 2 mm. So there may be reason to suppose that mid and high latitude regions of G1_S_hemisphere, because of the greater ice content, may supply amounts of gas equivalent in quantity to those less icy regions at equatorial latitudes. Variations in the mantle thickness have no effect on the flow in the viscous regime, a fact which is unphysical, particularly for mantle sizes on the order of a centimeter or more. In these cases, as expected, there is greater sublimation for cases of greater ice abundance, but all cases produce sufficient flux to compare well with the measured escape flux with only an order of magnitude difference between the maximum and the minimum flux produced.

Finally, the velocity and energy of a liberated water molecule as well as its time of flight and distance traversed in the atmosphere were calculated as if the molecules were liberated into a vacuum with no collisions during their atmospheric excursion, after Sieveka and

Johnson, [1982], and Hodges, [1973]. In the case of free sublimation to space, the velocity can be taken from Eq. 13, where the temperature of the liberated molecule is the temperature of the surface. In the case of Knudsen flow, the energy of the flow is lower because the molecules lose energy to the walls of the porous regolith. The departure velocity is that for the diffusion of molecules into a half space through a small orifice, namely the mean thermal speed. The departing molecules carry the temperature of the last object they touched, namely the walls of the porous regolith. In this formulation, with an angle of departure of 45° to the surface normal, free sublimation to space results in a time of flight of ~200 seconds and transit distances of 10s to hundreds of kilometers. Moreover in this gas flow regime, molecules may acquire sufficient energies upon liberation to escape; above surface temperatures of 110 K (~10:00-14:00 local time in the equatorial region) particles acquire energies in excess of the escape energy from Ganymede. In the Knudsen regime, particles do not acquire the energy to escape, times of flight may vary from 1 to 10 seconds depending upon the surface temperature, and distances traversed are on the order of meters.

6. A Diurnal Cycle

To simulate a hypothetical diurnal cycle, bestfit values of the sensitivity studies were used to construct the surface model. The albedo is as described in section 4, the terrain type was chosen by the criteria described in section 2. The porosity of the terrain was allowed to vary with local time in the following manner; local times from dawn to 08:00 were non-porous, local times from 08:00 to 10:00 were 20% porous, local times from 10:00 to 14:00 were 50% porous. This variability allowed a sampling of all the thermal regimes of the model. The gas flow regime was Knudsen flow unless δ was chosen to be less than 200 μm . The emissivity and mantle thickness were chosen such that temperatures in

certain grid cells matched the temperature data over the diurnal cycle, as determined in the sensitivity study. Thus emissivity increased and delta decreased as local times approached noon. In particular, delta for terrain type I was dropped to 20 μm in the 10:00 to 14:00 timeframe.

Results from this case are shown in figures 9-11. Figure 9 shows the surface temperature returned by the model. The model captures most of the major surface temperature non-uniformities seen in the data. The model does less well at capturing the temperatures at the extreme edges of G1_S_hemisphere, particularly the southernmost edge. It is in these regions where the PPR data are less reliable. The model also does less well as phase angles drift toward 90° . The figure shows that temperature differences between the model and the data are large at local times of approximately 10:00. This may be due to neglect of accurate phase function correction as discussed in section 5, or it may be due to surface properties which are heretofore unknown, such as a frost phase transition from amorphous to crystalline as the surface warms. Figure 10 shows the gas production rates and corresponding total production over a diurnal cycle. Total production is shown for comparative purposes with outgassing rates for other well known sublimating bodies. Total production for each cell is calculated from the gas production rate using an area corresponding to the spatial extent of the cell. The sum of the total production for each cell would yield the total production for the hemisphere. Maximum gas production seems to take place at local noon in equatorial latitudes regardless of the relative ice abundance within the terrain in cells at mid-latitudes. Figure 11 shows the modeled temperatures compared with data on a latitude by latitude basis. It is evident that the model is a poor match for data at latitudes below -60° .

7. Conclusions

We have developed a model for the temperature distribution on the surface of Ganymede. The model is based upon photometric properties of the surface determined from Voyager data, ground based constraints upon thermal inertia, very crude identifications of terrain composition and microtexture, but which incorporates considerations from gaskinetic theory used in modeling of cometary regoliths. This model can be readily adapted to incorporate photometric and microtextural properties of the surface as determined by Galileo when these results become available. The model has been used to infer diurnal temperature variations on the surface. These in turn have been used to infer the subliming flux of molecules upward into the atmosphere. Using the hypothetical diurnal cycle, we have shown that there may be a global gas production rate from upward sublimation of as much as 10^9 mol/cm²/s with a corresponding total production estimate of 10^{26} mol/s. A significant contribution to this flux comes at mid-latitudes from very icy terrains. The correlated total upward production is commensurate with the flux calculated for sputtering of 2×10^{26} mol/s [Paranicas, et al., in press, Ip, 1997]. Sublimation from the surface is not sufficiently energetic to excite water molecules to escape velocities, thus there may be a flux of cold water molecules near the surface which transit and rebound from the surface a number of times before recondensing. This process suggests the potential for molecular interaction with other uncondensed near surface molecules such as O₂, to build a cold atmospheric component near the surface. Photolysis in the atmosphere may dissociate and energize this component, since the photolysis process contains much more energy than that necessary to break the water bond. Since sputtering and sublimation are processes which peak in different latitude ranges and local times, the two mechanisms may combine to produce atmospheric constituents of compositions and energies which vary locally. Future work will examine the potential for this kind of interaction since at the distance of Ganymede from the sun, the time constant for photodissociation, 27 days, is much longer than a Ganymede diurnal cycle. Thus, if there is an interaction with other molecules near

the surface such that the time constant for residence of molecules in the atmosphere is long, results from this model suggest that there may be sufficient production of water, from sublimation alone, to supply the efflux measured by PLS.

There were a number of problems with the model, among them that the terrain was not truly locally segregated, we did not appropriately recondense material from the atmosphere to the surface, and we did not make use of a realistic model of the microtexture of the regolith. Thus these calculations are not truly self-consistent. This calculation may underestimate the amount of sublimation possible since there was no consideration of the efficacy of the solid state greenhouse effect [Uruquart and Jakosky, 1996]. Ion bombardment of the surface which results in the production of atmospheric gases leaves behind reactive radicals HO_2 and H_2O_2 in the surface ice [Bar-Nun et al., 1985]. If the uppermost surface layers of a regolith can be regarded as the "excited skin of the subaerial part of the ground", then this material seems ripe for further heterogeneous chemical processing with feedback to the atmosphere and surface. The chemical activity of this region of the regolith, presumed to be 20-200 μm by Noll et al., [1996] was not modeled.

In future work, the model will be based upon a more quantitative understanding of the terrain, one which will be obtained through data analysis. Future work will include identification of icy regions at better spatial resolution using NIMS data, a better understanding of the microtexture of the substrate from data analysis, true time-dependence in accounting for the condensation and refreezing of molecules from the atmosphere to the surface, and heterogeneous surface chemistry considerations.

References

- Bar-Nun A., G. Herman, M.L. Rappaport, and Yu Mekler, Ejection of H_2O , O_2 , H_2 and H from Water Ice by 0.5-6 keV H^+ and Ne^+ Ion Bombardment, *Surf. Sci.*, **150**, 143-156, 1985.
- Barth, C.A., C.W. Hord, A.I.F. Stewart, W.R. Pryor, K.E. Simmons, W.E. McClintock, J.M. Ajello, K.L. Nviaux, and J.J. Aiello, Galileo Ultraviolet Spectrometer Observations of Atomic Hydrogen in the Atmosphere of Ganymede, *Geophys. Res. Lett.*, **24**, 2147-2150, 1997.
- Belton, M.J.S., J.W. Head III, A.P. Ingersoll, R. Greeley, A.S. McEwen, K.P. Klaasen, D. Senske, R. Pappalardo, G. Collins, A.R. Vasavada, R. Sullivan, D. Simonelli, P. Geissler, M.H. Carr, M.E. Davies, J. Veverka, P.J. Gierasch, D. Banfield, M. Bell, C.R. Chapman, C. Anger, R. Greenberg, G. Neukum, C.B. Pilcher, R.F. Beebe, J.A. Burns, F. Fanale, W. Ip, T.V. Johnson, D. Morrison, J. Moore, G.S. Orton, P. Thomas, R.A. West, Galileo's First Images of Jupiter and the Galilean Satellites, *Science*, **274**, 377-385, 1996.
- Broadfoot, A.L., and the Voyager Ultraviolet Team, Overview of the Voyager ultraviolet spectrometry results through Jupiter encounter, *J. Geophys. Res.*, **86**, 8259, 1981.
- Brin G.D. and D.A. Mendis, Dust Release and Mantle Development in Comets, *Astrophys. J.*, **229**, 402-408, 1979.
- Buratti, B.J., R. Nelson, and A.L. Lane, Surficial Textures of the Galilean Satellites, *Nature*, **333**, 148-151, 1988.
- Buratti, B.J., Ganymede and Callisto: Surface Textural Dichotomies and Photometric Analysis, *Icarus*, **92**, 312-323, 1991.
- Carlson R., W. Smythe, K. Baines, E. Barbinis, K. Becker, R. Burns, S. Calcutt, W. Calvin, R. Clark, G. Danielson, A. Davies, P. Drossart, T. Encrenaz, F. Fanale, J. Granahan, G. Hansen, P. Herrera, C. Hibbitts, J. Hui, P. Irwin, T. Johnson, L. Kamp, H. Keiffer, F. Leader, E. Lellouch, R. Lopes-Gautier, D. Matson, t. McCord,

Acknowledgments: This report was prepared for the Jet Propulsion Laboratory, California Institute of Technology, sponsored by the National Aeronautics and Space Administration.

- R. Mehlman, A. Ocampo, G. Orton, M. Roos-Serote, M. Segura, J. Shirley, L. Soderblom, A. Stevenson, F. Taylor, J. Torson, A. Weir, P. Weissman, Near-Infrared Spectroscopy and Spectral Mapping of Jupiter and the Galilean Satellites: Results from Galileo's Initial Orbit *Science*, **274**, 385-388, 1996
- Cahill, D.G., S.K. Watson, and R.O. Pohl, Lower limit to the Thermal Conductivity of Disordered Crystals, *Phys. Rev. B*, **46**, 6131-6140, 1992.
- Calvin, W.M., R.E. Johnson, and J. R. Spencer, O₂ on Ganymede: Spectral Characteristics and Plasma Formation Mechanisms, *Geophys. Res. Lett.*, **23**, 673-676, 1996.
- Calvin, W.M., and J. R. Spencer, Latitudinal Distribution of O₂ on Ganymede: Observations with the Hubble Space Telescope, *Icarus*, **130**, 505-516, 1997.
- Cruikshank, D.P., R.H. Brown, W.M. Calvin, T.L. Roush, and M.J. Bartholomew, Ices on the Satellites of Jupiter, Saturn, and Uranus, *Solar System Ices*, B. Schmitt, M. Festou, and C. deBergh (eds.), Kluwer Academic Publishers, Dordrecht, 1997.
- Fountain J.A. and E.A. West, Thermal Conductivity of Particulate Basalt as a Function of Density in Simulated Lunar and Martian Environments, *J. Geophys. Res.*, **75**, 4063, 1970.
- Frank, L.A., W.R. Paterson, K.L. Ackerson, and S.J. Bolton, Outflow of Hydrogen Ions from Ganymede, *Geophys. Res. Lett.*, **24**, 2151-2154, 1997.
- Hall, D.T., P.D. Feldman, M.A. McGrath, and D.F. Strobel, The Far-ultraviolet Oxygen Airglow of Europa and Ganymede, *Astrophys. J.*, **499**, 475-481, 1998.
- Hansen, O.L., Ten-Micron Eclipse Observations of Io, Europa, and Ganymede, *Icarus*, **18**, 237-246, 1973.
- Hapke, B.W., A Theoretical Photometric Function for the Lunar Surface, *J. Geophys. Res.*, **68**, 4571-4586, 1963.
- Henry, L.G., and J.L. Greenstein, Diffuse Reflection by Planetary Atmospheres, *Astrophys. J.*, **93**, 70-87, 1941.

- Hodges, R.R., Helium and Hydrogen in the Lunar Atmosphere, *J. Geophys. Res.*, **78**, 8055-8064, 1973.
- Horanyi M, T.I. Gombosi, T.E. Cravens, A. Korosmezey, K. Kecskemety, A.F. Nagy, and K. Szego, The Friable Sponge Model of a Cometary Nucleus, *Astrophys. J.*, **278**, 449-455, 1984.
- Houppis, H.L., W.-H. Ip, and D.A. Mendis, The Chemical Differentiation of the Cometary Nucleus: The Process and its Consequences, *Astrophys. J.*, **295**, 654-667, 1985.
- Ip, W.-H., D.J. Williams, R.W. McEntire, and B. Mauk, Energetic Ion Sputtering Effects at Ganymede, *Geophys. Res. Lett.*, 1997.
- Kaviany M., *Principles of Heat Transfer in Porous Media*, Springer-Verlag, New York, 1991.
- Klinger J., Some Consequences of a Phase Transition of Water Ice on the Heat Balance of Cometary Nuclei, *Icarus*, **47**, 320-324, 1981.
- Kossacki, K.J., N.I. Komle., J. Leliwa-Kopystynki, and G. Kargi, Laboratory Investigation of the Evolution of Cometary Analogs: Results and Interpretation, *Planet. Space Sci.*, in press.
- Mason E.A. and A.P. Malinauskas, *Gas Transport in Porous Media; The Dusty-Gas Model*, Elsevier, New York, 1983.
- McCord, T.B., G.B. Hansen, R.N. Clark, P.D. Martin, C.A. Hibbitts, F.P. Fanale. J.C. Granahan, M. Segura, D.L. Matson, T.V. Johnson, R.W. Carlson, W.D. Smythe, G.E. Danielson, and the NIMS team, Non-water-ice constituents in the Surface Material of the icy Galilean Satellites from the Galileo Near-Infrared Mapping Spectrometer Investigation, *J. Geophys. Res.*, **103**, 8603-8626, 1998.
- McEwen, A.S., Photometric Functions for Photoclinometry and Other Applications, *Icarus*, **92**, 298-311, 1991.
- Morrison D., and D.P. Cruikshank, Thermal Properties of the Galilean Satellites, *Icarus*, **18**, 224-236, 1973.

- Newitt, D.M., M.U. Pai, and N.R. Kuloor, in *Thermodynamic Functions of Gases*, F. Din (ed.), Butterworth's Sci Pub., London, 102, 1956.
- Noll, K.S., R.E. Johnson, A.L. Lane, D.L. Dominique, and H.A. Weaver, Detection of Ozone on Ganymede, *Science*, **273**, 341-343, 1996.
- Orton, G.S., J.R. Spencer, L.D. Travis, T.Z. Martin, L.K. Tamppari, Galileo Photopolarimeter-Radiometer Observations of Jupiter and the Galilean Satellites *Science*, **274**, 389-391, 1996.
- Pappalardo, R. T., J.W. Head, G.C. Collins, L.M. Prockter, R. Greeley, C.R. Chapman, P. Helfenstein, G. Neukum, R. Wagner, and B.R. Tufts, Ganymede Tectonics: Insights from Galileo Imaging, *Bull. Am. Astron. Soc.*, **29**, 989, 1997.
- Paranicas C., W. R. Paterson, A. F. Cheng, B. H. Mauk, R. W. McEntire, L. A. Frank, and D. J. Williams, Low Energy Charged Particles Observed Near Ganymede, *J. Geophys. Res.*, in press.
- Present R.D., *Kinetic Theory of Gases*, McGraw-Hill, New York, 1958.
- Prockter, L.M., J.W. Head, R.T. Pappalardo, D. Senske, G. Neukum, R. Greeley, and J. Moore, Dark Terrain on Ganymede: New Observations from Galileo, *Bull. Am. Astron. Soc.*, **29**, 989, 1997.
- Sieveka, E.M., and R.E. Johnson, Thermal- and Plasma-Induced Molecular Redistribution on the Icy Satellites, *Icarus*, **51**, 528-548, 1982.
- Shi, M., R. A. Baragiola, D.E. Grosjean, R. E. Johnson, S. Jurac, and J. Schou, Sputtering of Water Ice Surfaces and the Production of Extended Neutral Atmospheres, *J. Geophys. Res.*, **100**, 26,387-26,395, 1995.
- Shizgal B.D., and A.G. Arkos, Nonthermal Escape of the Atmospheres of Venus, Earth, and Mars, *Rev. of Geophys.*, **34**, 483-505, 1996.
- Smoluchowski R., Heat Content and Evolution of Cometary Nuclei, *Icarus*, **47**, 312-319, 1981.

- Smoluchowski R., Heat Transport in Porous Cometary Nuclei, *J. Geophys. Res. A. Supp.*, **87**, 422-424, 1982.
- Smoluchowski R., Amorphous and Porous Ices in Cometary Nuclei, *Ices in the Solar System*, J. Klinger, D. Benest, A. Dolphus, and R. Smoluchowski (eds.), D. Reidel, Dordrecht, 397-406, 1985.
- Spencer, J.R., W.M. Calvin, and M.J. Person, Charge-coupled device spectra of the Galilean Satellites: Molecular Oxygen on Ganymede, *J. Geophys. Res.*, **100**, 19049-19056, 1995.
- Spencer, J.R., Thermal Segregation of water ice on the Galilean Satellites, *Icarus*, **69**, 297-313, 1987.
- Squyres, S.W., Surface Temperatures and Retention of H₂O Frost on Ganymede and Callisto, *Icarus*, **44**, 502-510, 1980.
- Squyres, S.W. and J. Veverka, Variation of Albedo with Solar Incidence Angle on Planetary Surfaces, *Icarus*, **50**, 115-122, 1982.
- Swinkels, F.B., and M.F. Ashby, A Second Report on Sintering Diagrams, *Acta Metallurgica*, **29**, 259-281, 1981.
- Uruquart, M.L. and B.M. Jakosky, Constraints on the Solid-state Greenhouse Effect on the Icy Galilean Satellites, *J. Geophys. Res.*, **101**, 21169-21176, 1996.
- Weitz, C.M., J.W. Head, R. Pappalardo, C. Chapman, R. Greeley, P. Helfenstein, and G. Neukum, Ganymede Impact Crater Morphology as Revealed by Galileo, *Bull. Am. Astron. Soc.*, **29**, 989, 1997.

Table 1: Free Parameters

	Terrain type 1	Terrain type 2	Terrain type 3
1.) terrain ice concentration (c_m)	100%	50%	20%
2.) porosity (ϕ)*	0%	20%	50%
<i>* varies with local time, not associated with terrain type</i>			
3.) Thermal conductivity* - an inverse function of temperature; f_x/T	f_1 0% poros	f_2 20% poros	f_3 50% poros
100% ice	1.1×10^3	4.5×10^2	7.2×10^1
50% ice	1.4×10^3	6.1×10^2	9.2×10^1
20% ice	9.1×10^2	3.7×10^2	5.6×10^1
<i>* constrained by eclipse thermal inertia data</i>			
	$r01$	$r02$	$r03$
4.) pore radius	0.75×10^4	1.0×10^4	10.0×10^4
5.) emissivity	0% poros	20% poros	50% poros
100% ice	1	1	1

50% ice	1	1	1
20% ice	1	1	1
for the sensitivity study emissivity values were: 1.0, 0.9, 0.8, 0.7, 0.6			

	free expansion into space (viscos flow)	Knudsen flow*
6.) gas flow regime	$\dot{Z} = nm\sqrt{\frac{\gamma kT}{m}}$	$\dot{Z} = N_p nm \frac{4}{3} \sqrt{\frac{2kT}{\pi m}}$
		*a function of porosity

7.) bulk density	$\rho_c = [(1 - c_m)\rho_{ic} + c_m\rho_d](1 - \phi)$

8.) Bond Albedo	$A_B = A_G f(\zeta) \left[2L(\zeta) \left(\frac{\cos i}{\cos i + \cos e} \right) + (1 - L(\zeta)) \cos i \right]$
	where $L(\zeta)$ is given in Table B and $f(\zeta) = 1$

	Δ_0	Δ_1	Δ_2	Δ_3	Δ_4	Δ_5
9.) mantle thickness	2 μm	20 μm	200 μm	0.2 cm	2.0 cm	20 cm

Table 2 - Phase angle dependence of the Limb darkening function L

Phase	
Angle	L

0	0.91
10	0.82
20	0.78
30	0.74
40	0.68
50	0.59
60	0.51
70	0.42
80	0.32
90	0.22
100	0.12
110	0.04
120-180	0.0

Figure Captions

figure 1: A Voyager map of Ganymede showing the outline of G1_S_hemisphere.

figure 2a: The figure shows NIMS spectra returned from the very icy Osiris Crater and also from the very dark Marius Regio region. These spectra show strong absorptions in the characteristic water ice bands of 1.5 μm and 2.0 μm at both Osiris and Marius Regio with relative differences. No absolute abundance is yet determined.

figure 2b - showing band depths of differing absorption features. Left: Voyager's camera. Middle: NIMS, showing water ice on the surface. Dark is less water, bright is more. Right: NIMS, showing the locations of minerals in red, and the size of ice grains in shades of blue. The mottled appearance indicates a terrain in which local ice abundance varies significantly.

figure 3. PPR surface brightness temperatures, and data, and one method of determining terrain type. The top left panel shows PPR surface brightness temperatures for the region designated G1_S_hemisphere. The gray scale shows the temperatures ranging from 80 K to 150 K as the surface encompasses local times from dawn to noon. The top right panel (3b) shows the corresponding temperatures contoured in a manner which allows comparison with the model. In these figures, 90° in local time corresponds to dawn, 180° to noon, and 270° to dusk. An initial calculation of surface temperature is shown in the bottom left panel (3c). These temperatures were subtracted from the PPR temperatures, and the difference is down in the bottom right panel (3d). Deviations from regular temperature striations in figure 3d indicate cold surface areas presumably composed of pure ice. An example of such a region is near the Osiris Crater, located near -40° latitude, 160° longitude.

figure 4: A global map similar to that of figure 1, showing the grid which was used for the model superimposed on contours of albedo. Separation of terrain type 2 from terrain type 3 was made roughly along the albedo contour of 0.25. Terrain type 1 was chosen for cells

with an albedo of 0.35 or greater which corresponded to the cold regions identified in the PPR data. (The overlay of the contours on the graphic requires more work).

figure 5 - Illustrates the effects of the Ganymede phase curve as described in equation 16 which corrects from geometric or normal albedo to Bond albedo. The phase curve lowers the albedo at high phase angles and raises the albedo at small phase angles. The phase curve also raises the normal albedo at high latitudes where the incidence angle is low. The correction accounts for specific scattering properties of the Ganymede surface as a function of local time.

figure 6 The top panel shows Voyager geometric albedos derived from the PDS clear filter (0.47 μm). The bottom panel shows the bond albedo with the phase correction applied. Surface bond albedos show a saddle around local noon.

figure 7 - The temperature dependent thermal conductivities derived for the model, shown in figure 7c, and some of the intermediate functions which were part of the calculation (see Eq. 4). One is the variation in the thermal conductivity of the icy portion of the conglomerate with temperature. Two is the variation in the thermal conductivity of the rocky portion of the conglomerate with rock concentration. Two is temperature invariant. The derived thermal inertia for each case is shown in figure 7d along with those derived from ground based radiometry data (solid black line). The first set of numbers in each label refers to the porosity of the conglomerate where 00 designates 0% porous, 20 means 20% porous, etc. The second set of numbers refers to the concentration of ice in the conglomerate, where 00 designates 100% ice, 50 is 50% ice, etc. The figure illustrates that the model thermal conductivity is not a linear relationship with ice content. The effective conductivity drops uniformly as the porosity increases, but since the conglomerate density increases rapidly with increasing rock content, the effective conductivity of a conglomerate composed of 50% ice is larger than either of the other cases involving different ice composition.

figure 8a - The surface temperature, gas flux, and total production are compared for various test cases of the model. In figure 8a the maximum temperature, gas flux, and total production for cases of the same terrain type (terrain type I), but different gas flux regimes, thermal (porosity) regimes, and differing mantle thicknesses are compared. The heavy black line indicates PPR maximum surface temperatures, and PLS measured escape flux, respectively.

figure 8b - The maximum temperature, gas flux, and total production for cases of the same thermal (porosity) regimes (50% porosity), but different gas flux regimes, terrain type, and differing mantle thicknesses are compared.

figure 9 - The top panel shows a surface plot of the PPR surface temperatures for G1_S_hemisphere (the projection of the contours in the top portion of the box is identical to those of figure 3b). The middle panel shows a surface plot of the surface temperatures found by the model. The bottom panel shows a surface plot of the differences between the model and the data. Differences are close to zero at most latitudes and longitudes, but are very large near the south pole and near dawn where the phase correction is weakly known.

figure 10 - The top panel shows the gas flux, and the bottom panel shows the corresponding total production for a model of gas flow in the Knudsen regime. The areal multiplicative factor from which the total production is derived is the size of the grid section.

figure 11 - A latitude comparison of the modeled temperatures (dashed), with the PPR data (solid). At southernmost latitudes the actual temperatures may be anomalously high. At mid and equatorial latitudes the model captures the large scale dips in temperature very well. Fine scale adjustments to the model included the emissivity and thickness of mantle overlayer.

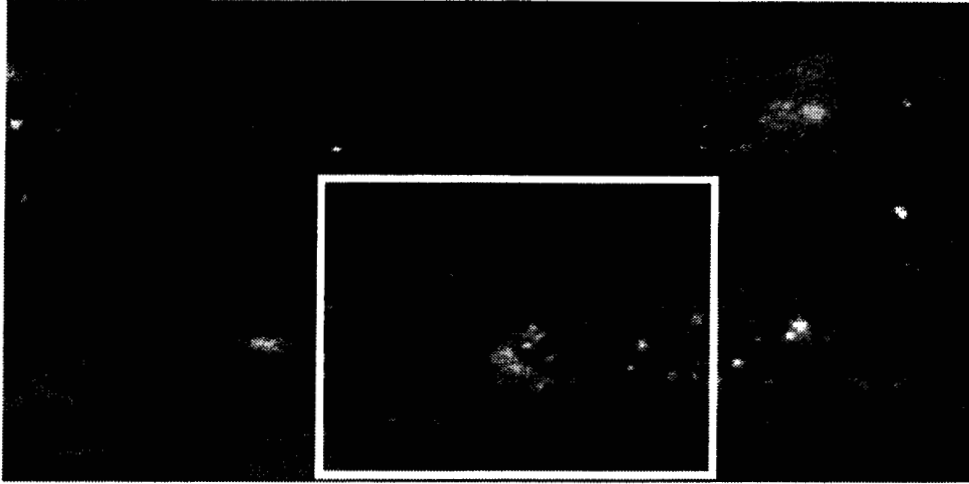


figure 1. A Voyager map of Ganymede showing the outline of G1_S_hemisphere.

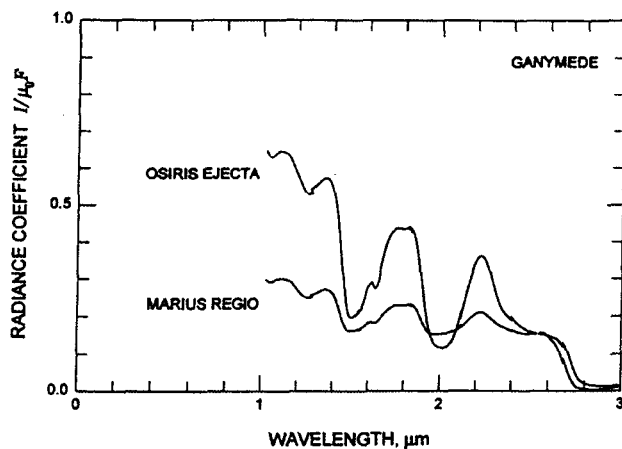
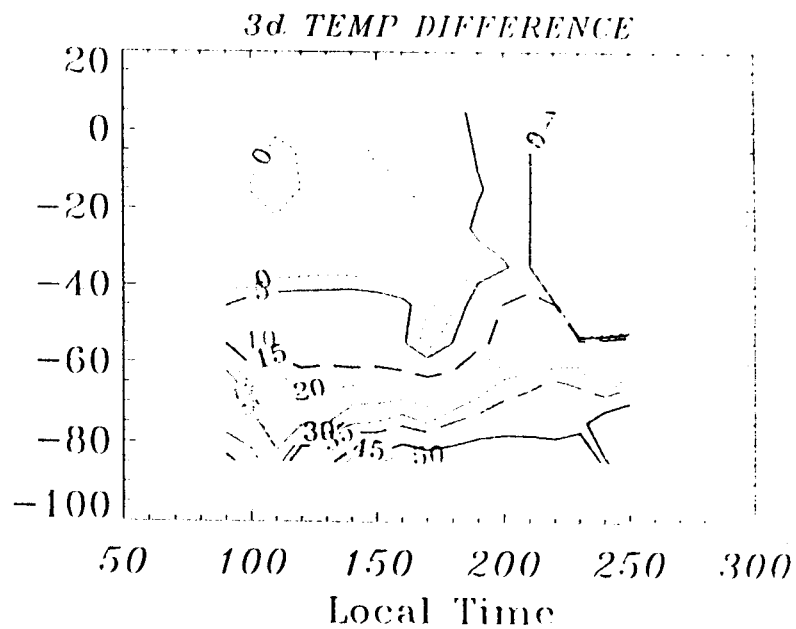
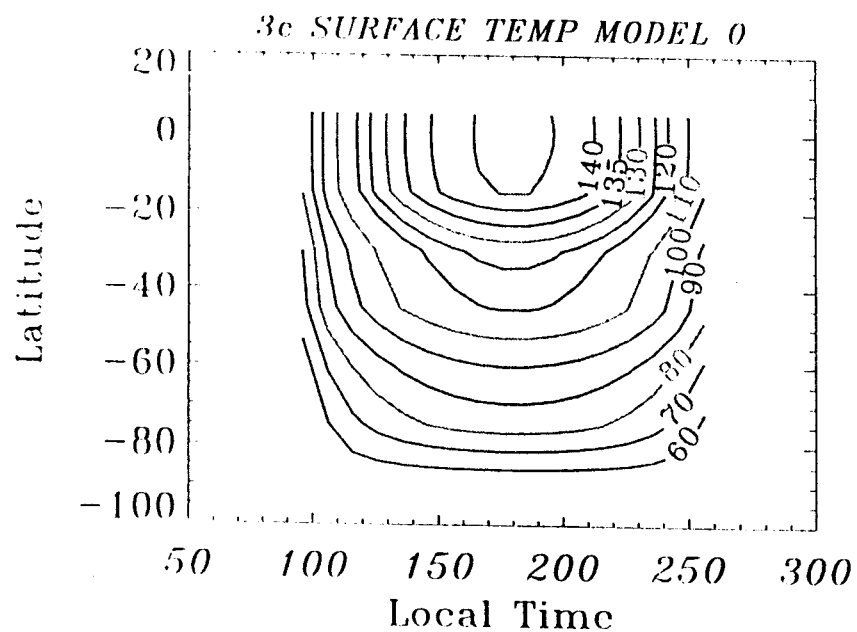
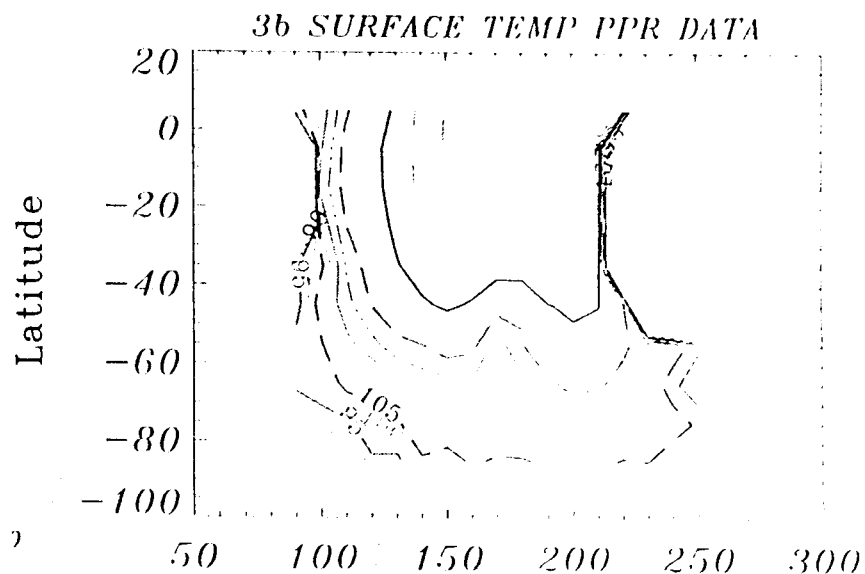
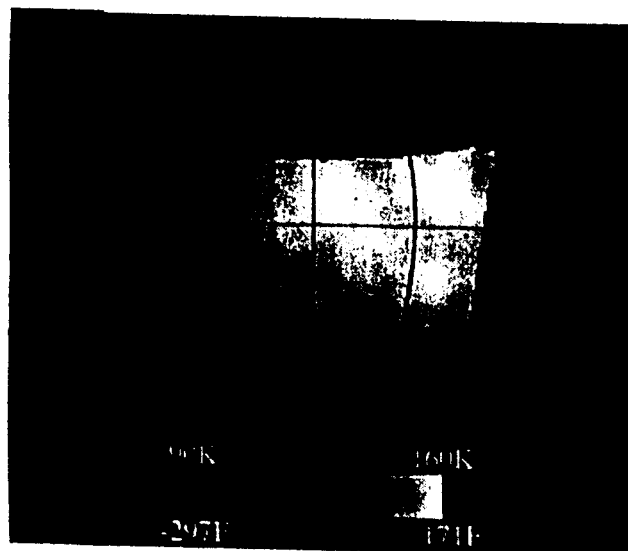
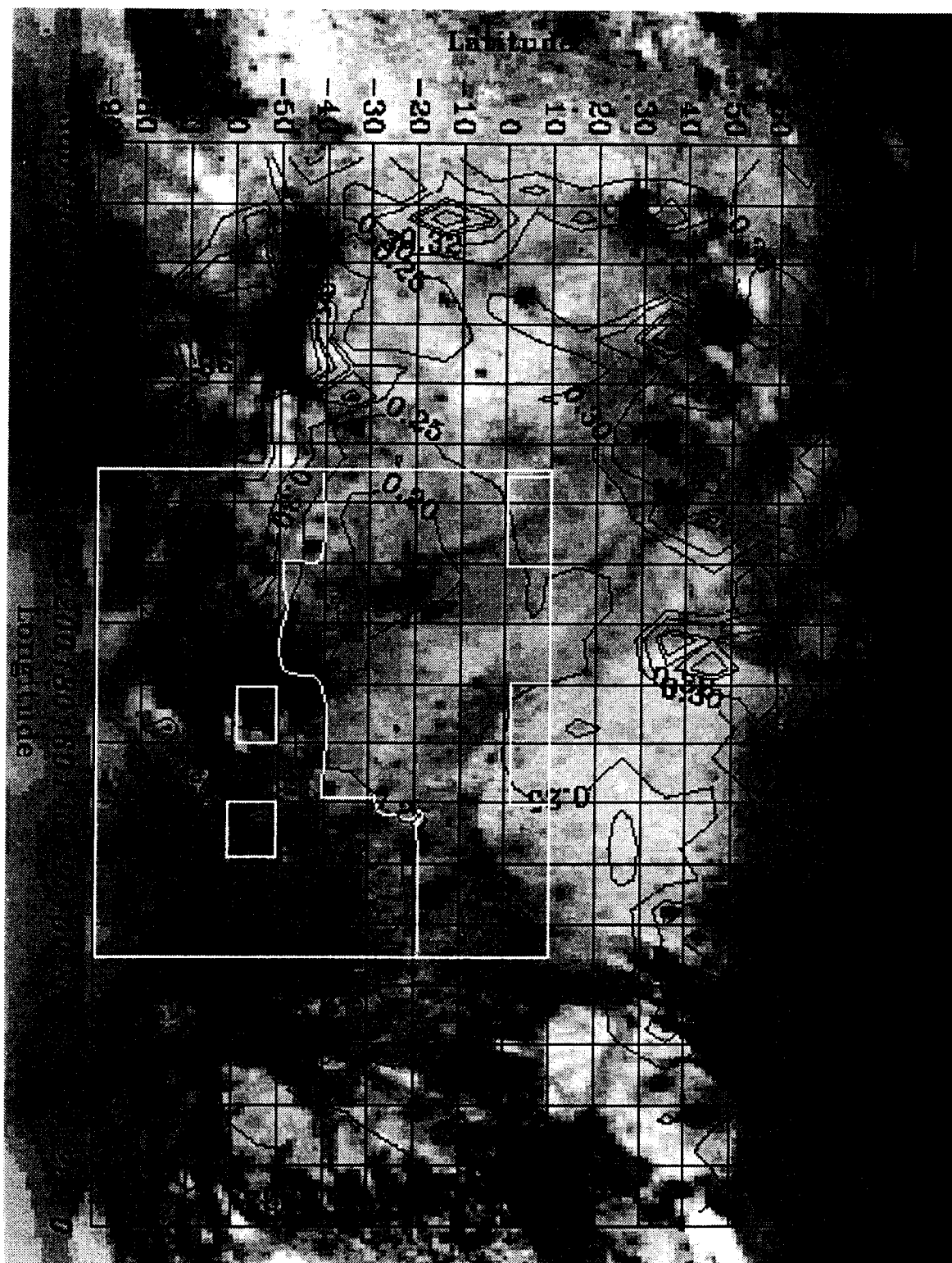


figure 2a. The figure shows NIMS spectra returned from the very icy Osiris Crater and also from the very dark Marius Regio region. These spectra show strong absorptions in the characteristic water ice bands of 1.5 μm and 2.0 μm at both Osiris and Marius Regio. Ice absorption takes place in both terrain extremes, with relative differences, but no absolute abundance is yet determined.



Figure 2b - showing band depths of differing absorption features. Left: Voyager's camera. Middle: NIMS, showing water ice on the surface. Dark is less water, bright is more. Right: NIMS, showing the locations of minerals in red, and the size of ice grains in shades of blue. The mottled appearance indicates a terrain in which local ice abundance varies significantly.





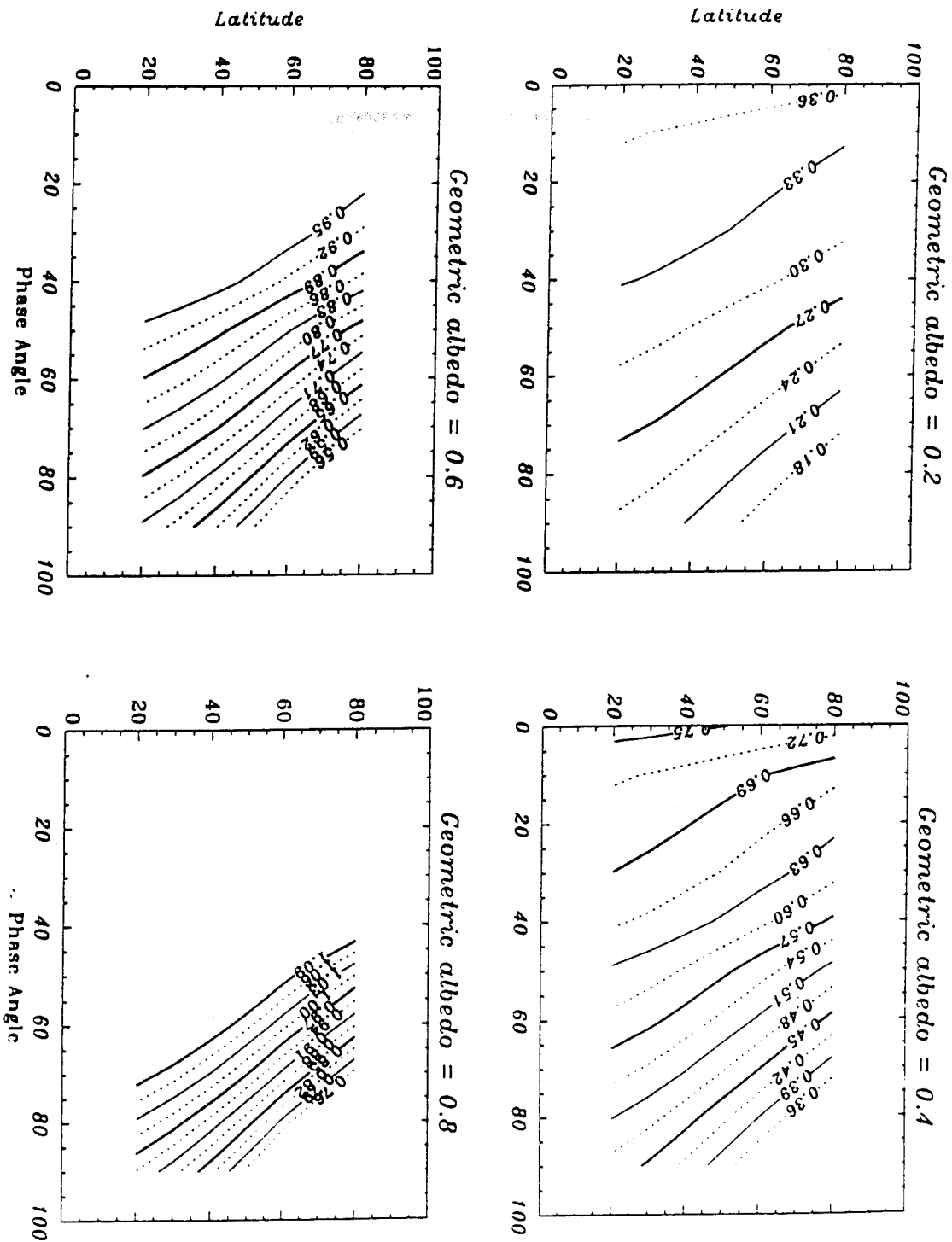


Figure 5 - Illustrates the effects of the Ganymede phase curve as described in equation 16 which corrects from geometric or normal albedo to Bond albedo. The phase curve lowers the albedo at high phase angles and raises the albedo at small phase angles. The phase curve also raises the normal albedo at high latitudes where the incidence angle is low. The correction accounts for specific scattering properties of the Ganymede surface as a function of local time.

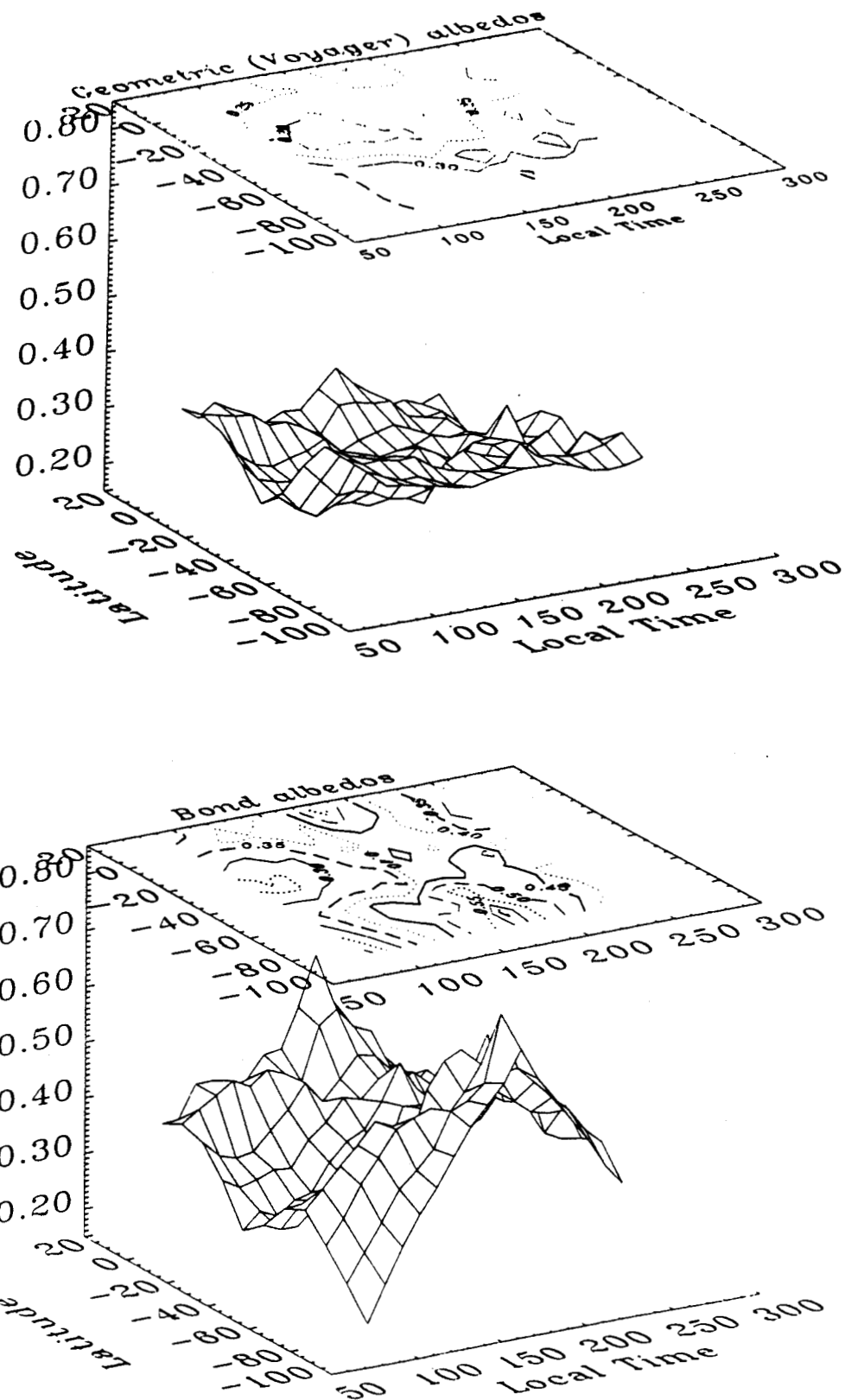


Figure 6 The top panel shows Voyager geometric albedos derived from the PDS clear filter ($0.47\ \mu\text{m}$). The bottom panel shows the bond albedo with the phase correction applied. Surface bond albedos show a saddle around local noon.

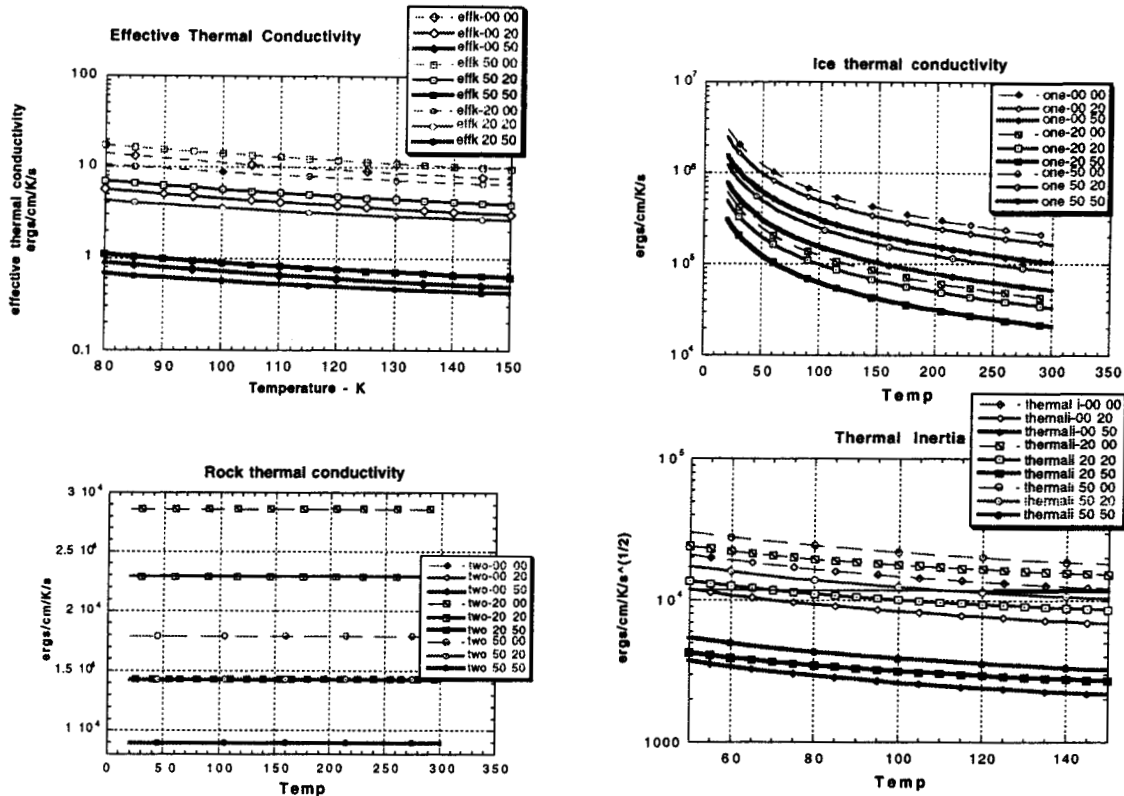


Figure 7 - The temperature dependant thermal conductivities derived for the model, shown in figure 7c, and some of the intermediate functions which were part of the calculation (see equation 4). One is the variation in the thermal conductivity of the icy portion of the conglomerate with temperature. Two is the variation in the thermal conductivity of the rocky portion of the conglomerate with rock concentration. Two is temperature invariant. The derived thermal inertia for each case is shown in figure 7d along with those derived from ground based radiometry data (solid black line). The first set of numbers in each label refers to the porosity of the conglomerate where 00 designates 0% porous, 20 means 20% porous, etc. The second set of numbers refers to the concentration of ice in the conglomerate, where 00 designates 100% ice, 50 is 50% ice, etc. The figure illustrates that the model thermal conductivity is not a linear relationship with ice content. The effective conductivity drops uniformly as the porosity increases, but since the conglomerate density increases rapidly with increasing rock content, the effective conductivity of a conglomerate composed of 50% ice is larger than either of the other cases involving different ice composition.

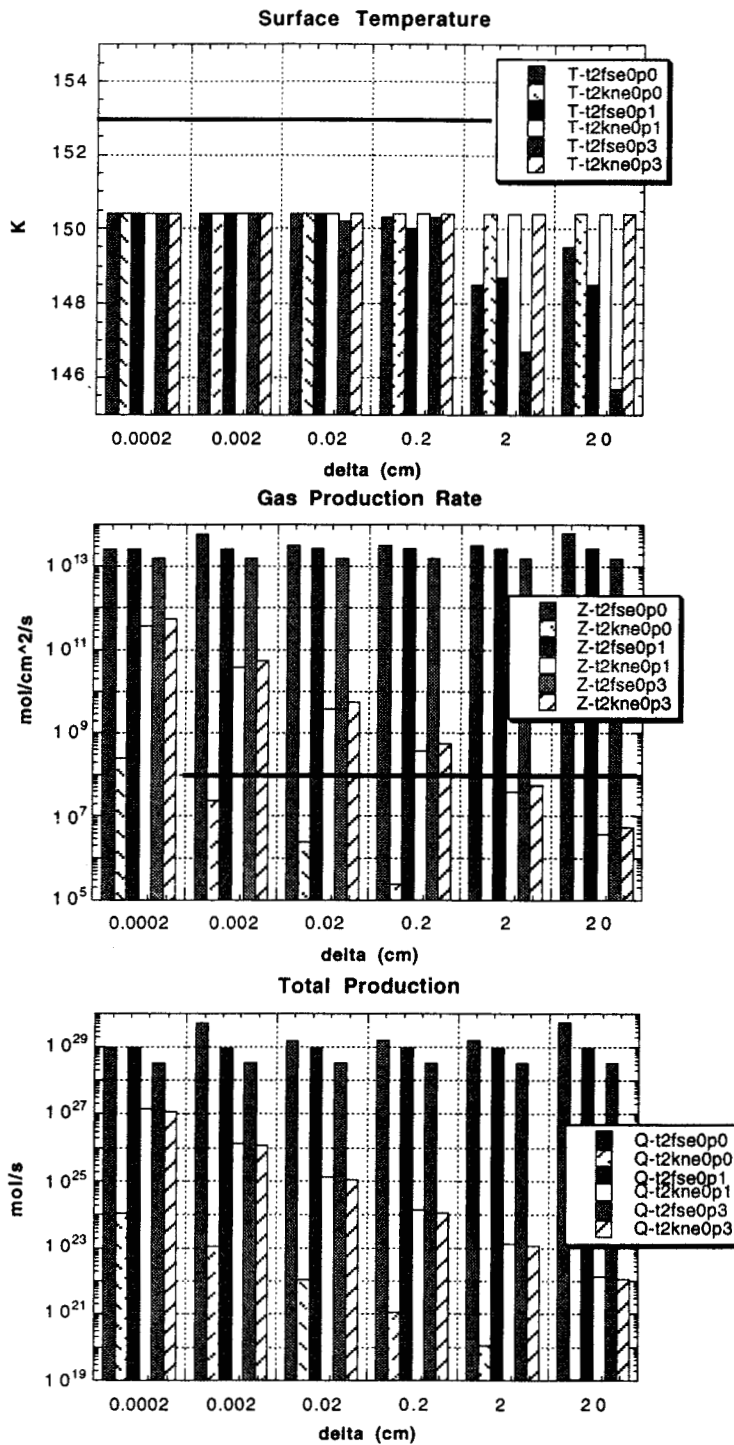


Figure 8a - The surface temperature, gas flux, and total production are compared for various test cases of the model. The heavy black line indicates PPR maximum surface temperatures, and PLS measured escape flux, respectively. Porosity increases to the right for each mantle size scale. Solid coloring indicates the viscous gas flow regime. For small delta and large porosity, the Knudsen gas production approaches that for the viscous regime.

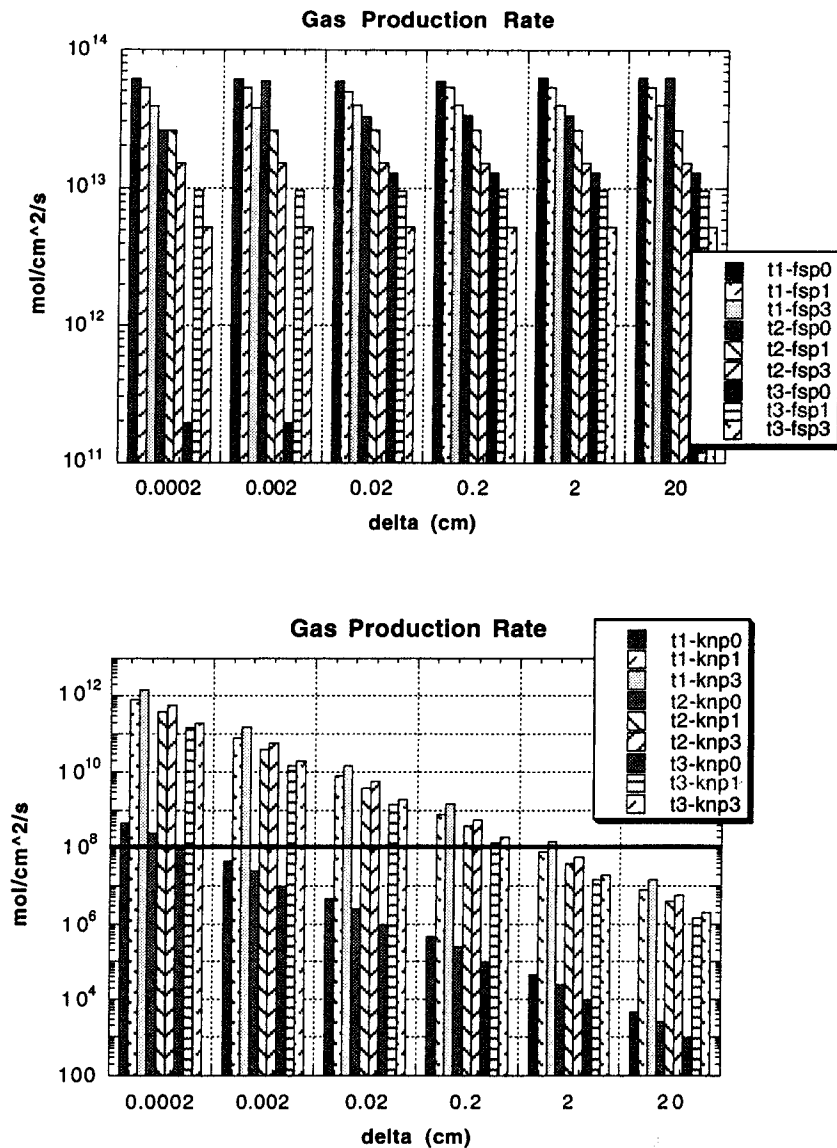
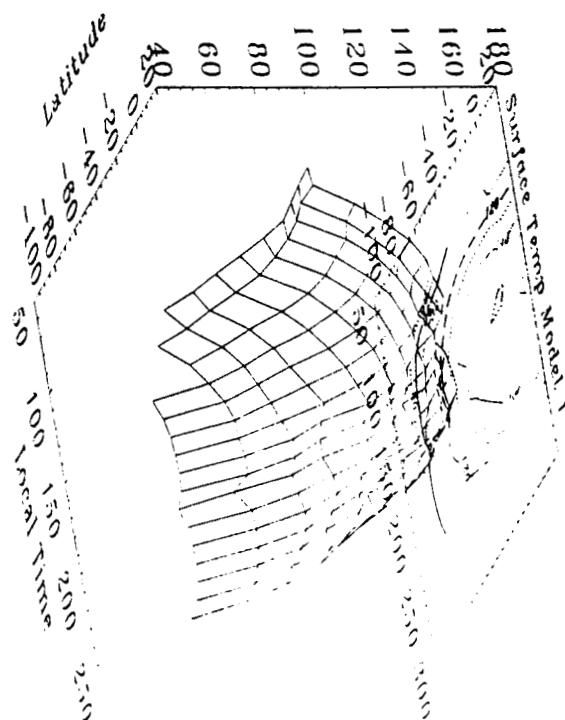
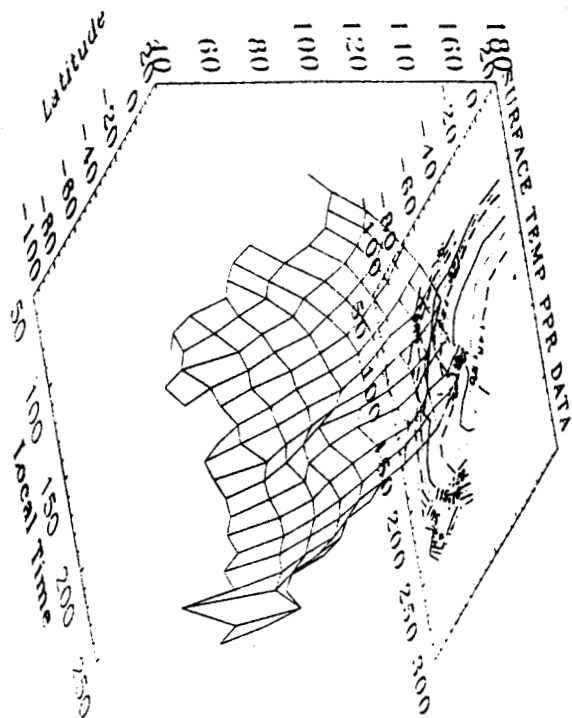
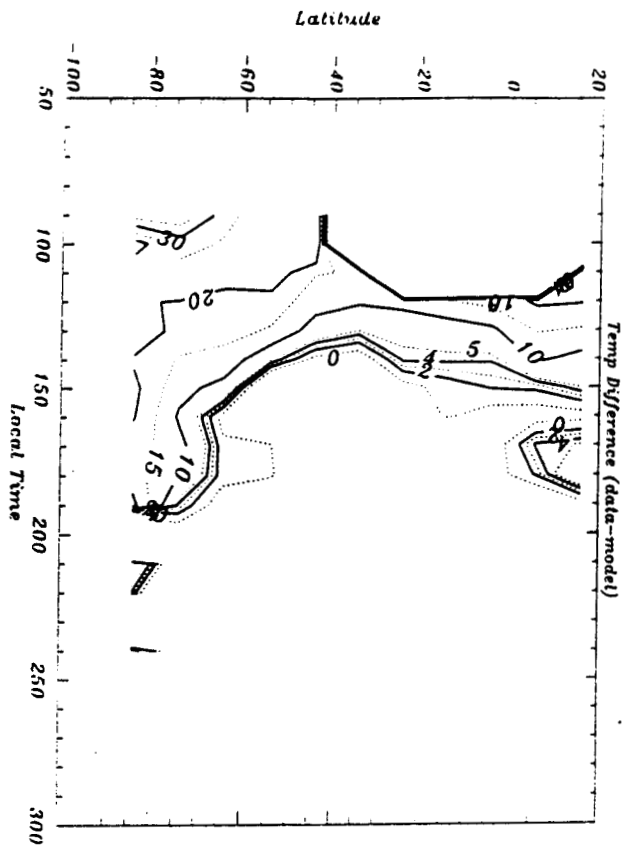
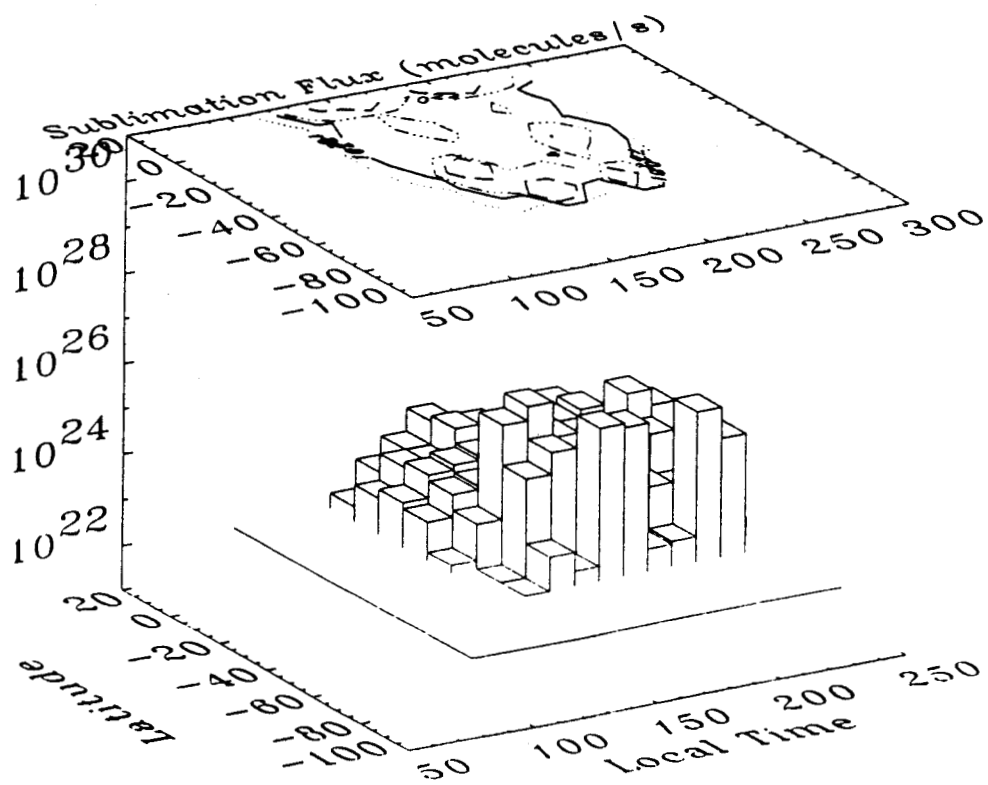
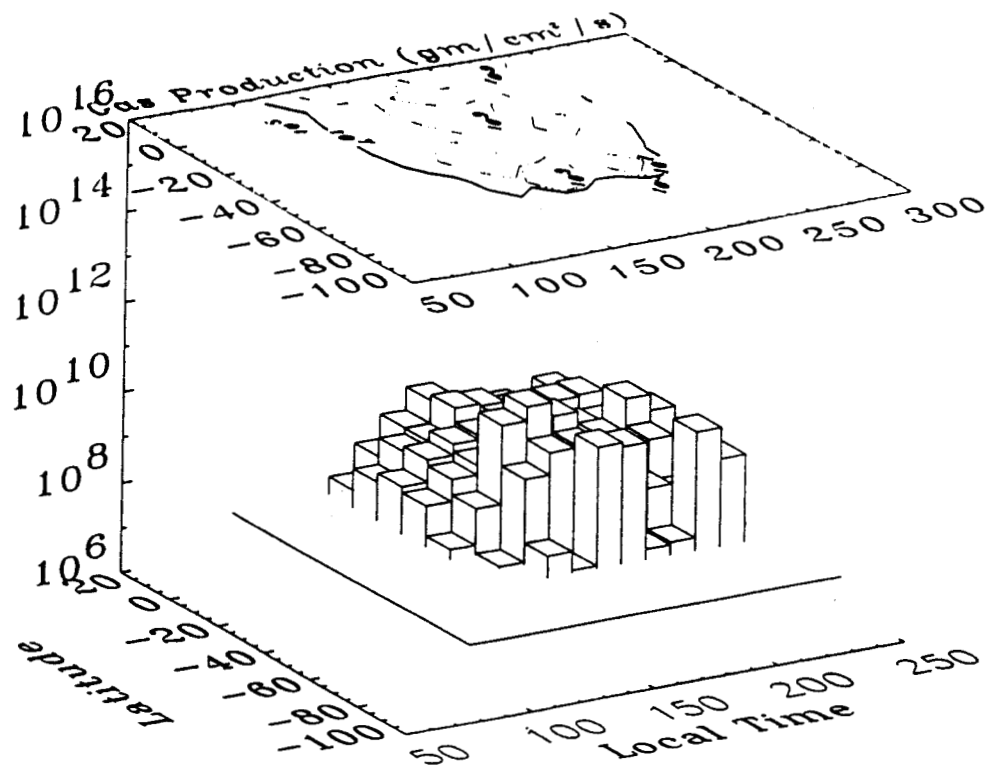


Figure 8b - The maximum gas production for cases of differing thermal (porosity) regimes, gas flux regimes, terrain type, and differing mantle thicknesses are compared. The top panel shows the viscous regime (free sublimation to space), the bottom panel shows the Knudsen regime (free molecular flow). The non-porous cases are indicated with solid coloring. Ice content increases to the left within each mantle size scale. The size of the mantle is irrelevant to the viscous regime, while in the Knudsen regime, gas production is reduced as the mantle thickness increases. In the viscous regime there is only an order of magnitude difference in the quantity of gas produced in all cases, while in the Knudsen regime gas production can be cut by up to 6 orders of magnitude with increases in mantle thickness, ice content, or porosity.





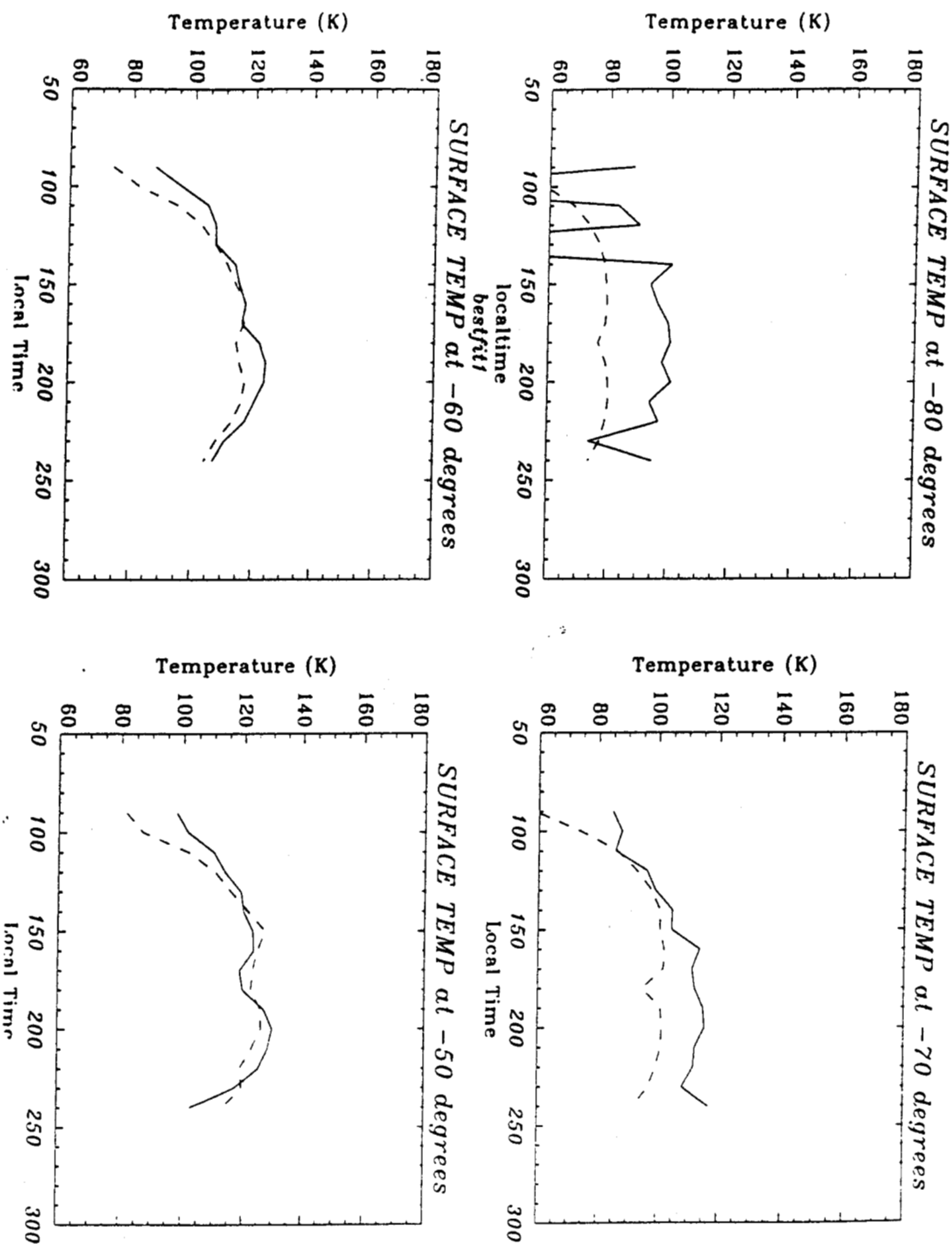


Figure 11 - A latitude comparison of the modeled temperatures (dashed), with the PPR data (solid). At southernmost latitudes the actual temperatures may be anomalously high. At mid and equatorial latitudes the model captures the large scale dips in temperature very well. Fine scale adjustments to the model included the emissivity and thickness of mantle overlayer.

